Activity-dependent dendritic spine neck changes are correlated with synaptic strength

Roberto Araya[a,b,1], Tim P. Vogels[a,c], and Rafael Yuste[a]

[a]Department of Biological Sciences, Columbia University, New York, NY 10027; [b]Department of Neurosciences, Faculty of Medicine, University of Montreal, Montreal, QC, Canada H3C 3J7; and [c]Centre for Neural Circuits and Behaviour, Department of Physiology, Anatomy, and Genetics, University of Oxford, Oxford OX1 3SR, United Kingdom

Edited by Rodolfo R. Llinas, New York University School of Medicine, New York, NY, and approved June 3, 2014 (received for review November 22, 2013)

Most excitatory inputs in the mammalian brain are made on dendritic spines, rather than on dendritic shafts. Spines compartmentalize calcium, and this biochemical isolation can underlie input-specific synaptic plasticity, providing a *raison d'etre* for spines. However, recent results indicate that the spine can experience a membrane potential different from that in the parent dendrite, as though the spine neck electrically isolated the spine. Here we use two-photon calcium imaging of mouse neocortical pyramidal neurons to analyze the correlation between the morphologies of spines activated under minimal synaptic stimulation and the excitatory postsynaptic potentials they generate. We find that excitatory postsynaptic potential amplitudes are inversely correlated with spine neck lengths. Furthermore, a spike timing-dependent plasticity protocol, in which two-photon glutamate uncaging over a spine is paired with postsynaptic spikes, produces rapid shrinkage of the spine neck and concomitant increases in the amplitude of the evoked spine potentials. Using numerical simulations, we explore the parameter regimes for the spine neck resistance and synaptic conductance changes necessary to explain our observations. Our data, directly correlating synaptic and morphological plasticity, imply that long-necked spines have small or negligible somatic voltage contributions, but that, upon synaptic stimulation paired with postsynaptic activity, they can shorten their necks and increase synaptic efficacy, thus changing the input/output gain of pyramidal neurons.

STDP | neocortex | basal dendrites

Dendritic spines are found in neurons throughout the central nervous system (1), and in pyramidal neurons receive the majority of excitatory inputs, whereas dendritic shafts are normally devoid of glutamatergic synapses (2–7). These facts suggest that spines are likely to play an essential role in neural circuits (1), although it is still unclear exactly what this role is (8, 9). Because of their peculiar morphology, hypotheses regarding the specific function of spines have focused on their role in biochemical compartmentalization, whereby a small spine head, where the excitatory synapse is located, is separated from the parent dendrite by a thin neck, isolating the spine cytoplasm from the dendrite (10). Indeed, spines are diffusionally restricted from dendrites (11–13) and compartmentalize calcium after synaptic stimulation (14–16). This local biochemistry and the high calcium accumulations observed following temporal pairing of neuronal input and output (14, 17, 18) are thought to be responsible for input-specific synaptic plasticity (19–21). However, besides this biochemical role, spines have also been hypothesized to play an electrical role, altering excitatory postsynaptic potentials (EPSPs) (22–30). Consistent with this idea, activating spines with two-photon uncaging of glutamate generates potentials whose amplitudes are inversely proportional to the length of the spine neck (31), and these responses are much larger in spines than in adjacent dendritic shafts (32). Also, spine conductances can be activated independently of dendritic ones (33–36). These data suggest that spines could serve as electrical compartments but, at the same time, raise the issue of the functional significance of the thousands of long-necked spines that cover the dendrites of pyramidal neurons, which would therefore have negligible somatic voltage contributions.

In this study we first undertook a series of experiments to discern the potential effect that the spine neck length has on the synaptic potentials generated by minimal synaptic stimulation at identified spines. We find that EPSP amplitudes are inversely correlated with spine neck lengths and that, as also seen in glutamate uncaging experiments (31), long-necked spines do not appear to generate any significant somatic depolarizations. In a separate set of experiments, we used a spike timing-dependent long-term potentiation (STD-LTP) induction protocol to trigger rapid shortening of the stimulated spine neck, which was accompanied by increases in the amplitude of the evoked potentials. In essence, we thus found a way to rapidly increase the voltage contribution of long-necked spines. To dissect the plausible mechanisms of the effect, we conducted biophysical simulations in the software NEURON. Our models show that the observed phenomenon could be accounted for by rapid regulation of synaptic conductance or, alternatively, stem from electrical attenuation effects due to the changes in spine neck resistance associated with changes in neck length. The spine neck resistance values necessary to entirely account for such attenuation are at odds with reported estimates (13, 32), so one would be inclined to assume that a rapid increase in synaptic conductance leads to the observed changes in somatic EPSP size. However, because spine neck resistance values have so far been inferred only indirectly, one cannot rule out the possibility that a combination of (synaptic) conductance and (neck) resistance changes could contribute to the observed activity-dependent changes in somatic EPSP size.

Significance

Dendritic spines are the main recipients of excitatory information in the brain, and though it is accepted that they must serve an essential function in neural circuits, their precise role remains ill-defined. Here, using minimal synaptic stimulation, we show that spine neck length correlates inversely with synaptic efficacy. In addition, we discovered a previously unidentified form of spine plasticity following a spike timing-dependent plasticity protocol, characterized by rapid shortening of spine neck length and concomitant increases in synaptic strength. These results provide new insights for our understanding of synaptic plasticity, and could provide an explanation for the presence of thousands of long-necked spines in the dendrites of pyramidal neurons, whose somatic synaptic contribution would otherwise be small or negligible.

Author contributions: R.A. and R.Y. designed research; R.A. and T.P.V. performed research; R.A. and T.P.V. analyzed data; and R.A., T.P.V., and R.Y. wrote the paper.

The authors declare no conflict of interest.

This article is a PNAS Direct Submission.

[1]To whom correspondence should be addressed. Email: roberto.araya@umontreal.ca.

This article contains supporting information online at www.pnas.org/lookup/suppl/doi:10.1073/pnas.1321869111/-/DCSupplemental.

Results

Imaging Spines Under Minimal Stimulation EPSPs. To explore the relation between EPSPs and the morphology of the spine neck, we studied spines located in the proximal region of basal dendrites of layer-5 pyramidal neurons in slices from mouse primary visual cortex (Fig. 1; *Materials and Methods*). Neurons were filled with a calcium indicator, and two-photon line scans were performed through spines located close to an extracellular stimulating electrode (~4–20 μm), allowing us to detect spines activated by brief extracellular electrical stimuli (14, 16–18) (Fig. 1*C*). To preserve normal synaptic transmission, experiments were performed with standard artificial cerebrospinal fluid (ACSF) containing 2 mM Ca^{2+} and 2 mM Mg^{2+}. Voltage responses to these extracellular stimuli were simultaneously recorded at the soma of the imaged cell with a patch electrode (Fig. 1 *A1*, *C2*, and *C3*). After carefully searching neighboring dendrites, we detected spines with $[Ca^{2+}]_i$ increases time-locked to the extracellular stimulation, suggesting they were mediating synaptic responses generated by the activation of neighboring axons. Indeed, these calcium accumulations were completely and reversibly blocked by NMDA and AMPA receptor blockers (Fig. 1 *B2* and *B3*; control = 35% ΔF/F; in CNQX + APV = 0.3% ΔF/F; washout = 40.9% ΔF/F), indicating that they were the result of glutamate released from presynaptic terminals rather than from direct electrical activation of spine receptors or postsynaptic membranes (14, 16–18).

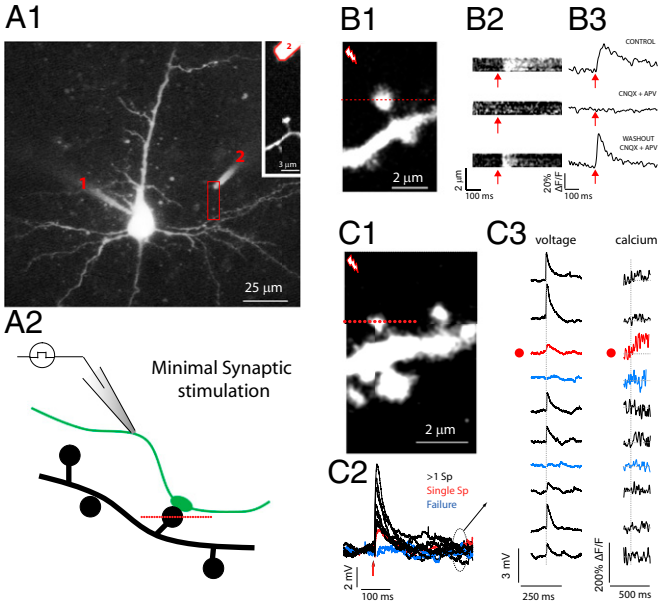

Fig. 1. Spine responses to minimal stimulation. (*A1*) A layer-5 pyramidal cell loaded with Alexa 488 (200 μM) and fluo-4 (200 μM) with a patch electrode (1). A stimulating electrode (2) filled with Alexa 594 dextran (10,000 MW, 50 μM), was located close (~4–20 μm) to spines of basal dendrites to increase the likelihood of activating an axon contacting the imaged spine. (*A2*) Diagram of the experiment. Brief current pulses were delivered to a stimulating electrode while voltage responses (recorded at the soma) and calcium signals (fluorescence signal arising from line scans intersecting the spine head) were simultaneously imaged. (*B1*) Two-photon fluorescent image of a spine from an experiment similar to the one shown in *A1*. (*B2*) Average of line scans through the spine head shown in 1 before (*Top*) and after (*Middle*) perfusion with the NMDA and AMPA receptor antagonist DL-2-amino-5-phosphonopentanoic acid (D-APV) (40 μM) and 6-cyano-7-nitroquinoxaline-2,3-dione (CNQX) (10 μM), respectively, and after washout (*Bottom*). (*B3*) Calcium accumulations under the three conditions shown in *B2*. (*C1*) The spine intersected by a red dotted line in the fluorescence image was imaged while stimulating a nearby axon. (*C2*) voltage traces recorded after minimal synaptic stimulation of the spine crossed by a red dotted line in *C1*. Failures (blue), minimal (red), and bigger-than-minimal voltage responses (black) were evident. (*C3*) Sequence of voltage traces and calcium signals recorded from the spine head. Note that the minimal voltage response corresponded with a clear calcium response from the imaged spine head (red dot and red traces).

In an effort to isolate the somatic voltage contribution of individual spines, the stimulation intensity was set to the minimal strength that still generated a calcium accumulation at the imaged spine head. At these intensities, identical stimulations elicited EPSPs of different amplitudes, including failures, as expected from the stochastic nature of synaptic transmission (Fig. 1 *C2*). To identify somatic EPSPs that are likely to be generated by individual spines, for each experiment we selected the trial in which we observed the smallest EPSP response that was still associated with a clear calcium accumulation at the imaged spine head (Fig. 1 *C2* and *C3*, red traces). Under these minimal stimulation conditions, the imaged spine is likely the only one activated in the dendritic tree (14, 18, 37–42). Consistent with this, we observed concomitant failures of EPSPs and spine calcium accumulations (Fig. 1 *C2* and *C3*, blue traces). In agreement with the possibility that these were single-spine responses, somatic voltages associated with these "minimal" responses were consistent with the amplitude of previously recorded single-spine EPSPs extracted from paired recordings (43), with quantal analysis measurements of single-input activation (14, 18, 44), and with potentials measured after uncaging glutamate at individual spines (31, 45, 46). Trials with larger voltage responses (Fig. 1 *C2* and *C3*, black traces), which probably represent the simultaneous activation of multiple spines, were discarded from our analysis.

Inverse Correlation Between Spine Neck Length and Synaptic Potential. We then searched our dataset for potential correlations between the morphologies of individual spines and the EPSPs they generated. To prevent biases in the analysis, we devised an automatic algorithm that blindly and independently scored the calcium and voltage responses to minimal stimulation (Fig. S1). From all data (334 trials from 22 spines from 16 neurons), the algorithm selected 29 responses from 12 spines (from 10 neurons) with significant calcium responses, as defined by meeting three independent statistical criteria (Fig. S1*F*, red dots; *Materials and Methods*), and measured the amplitude of their corresponding EPSPs. From all of the trials with positive calcium responses, only trials with minimal or zero amplitude EPSPs were selected. In these spines we then quantified the spine head diameter and neck length—measured from 3D stacks of images—and correlated both variables with the peak amplitude and rate of rise of their corresponding EPSPs (Figs. S1*E* and S2). Morphological features of the spines were measured blindly with respect to their electrical responses. In this analysis, we found a strong negative correlation between the amplitude of the voltage responses and the spine neck lengths. Stimulation of spines with short necks reliably generated larger EPSPs (Fig. 2*A*), whereas spines with longer necks had mostly smaller, or undetectable, voltage responses (Fig. 2 *B* and *C*, red dots). A linear fit of the amplitude vs. neck length data gave an r^2 value of 0.52 (with a P value <0.01) and an rms error (RMSE) of 0.29 mV. A quadratic fit to the voltage divider equation (*Materials and Methods*) provided a similarly good fit (rmse 0.19 mV; see below for electrical model). These data from minimal synaptic stimulation of spines were virtually indistinguishable from those obtained with two-photon uncaging of glutamate at individual spines (31) (Fig. 2*C*, gray dots, each of which corresponds to the average uncaging response measured from independent spines) with similar error values (rmse 0.26 mV and 0.27 mV for linear and quadratic power law fit, respectively). Using a cutoff of 1.5 μm for spine neck lengths, we also demonstrated a significant difference ($P < 0.05$) in the response amplitude of long-necked spines (0.15 ± 0.09 mV; $n = 6$ spines, for electrical stimulation and 0.11 ± 0.05 mV; $n = 9$ spines for uncaging stimulation) compared with short-necked spines (0.64 ± 0.19 mV; $n = 6$ spines for electrical and

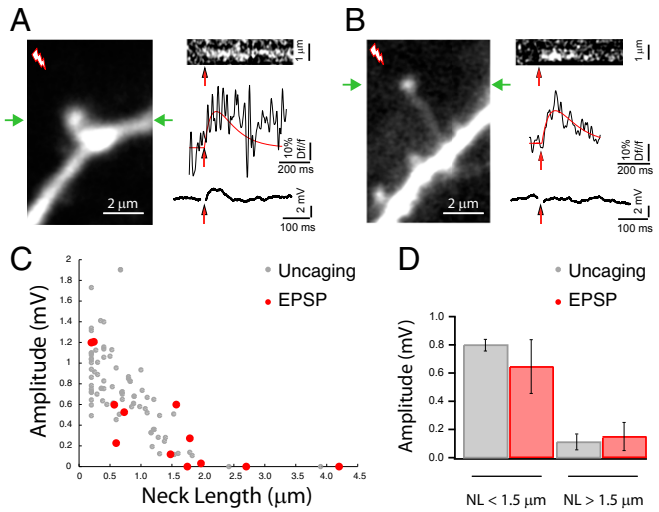

Fig. 2. Inverse correlation between EPSP amplitude and spine neck length. (*A*) Synaptic activation of a short-necked spine generated a clear calcium response at the spine head and a clear minimal stimulation voltage deflection at the soma. (*B*) Synaptic activation of a single long-necked spine generated a clear calcium response at its head, but no voltage deflection at the soma. Green arrows in *A* and *B* mark the line scan intersecting the spine head. (*C*) Amplitude of the voltage response generated by minimal stimulation in a spine plotted vs. neck length (red dots), and uncaging potential amplitudes plotted vs. neck length (46) (gray dots). (*D*) Graph shows that the amplitude of voltage responses from short-necked spines (neck length <1.5 μm) is significantly reduced ($P < 0.01$) relative to long-necked spines (neck length >1.5 μm) upon activation by minimal stimulation (red bars) or two-photon uncaging of glutamate (gray bars), and no statistical difference was detected between uncaging and minimal stimulation synaptic responses (see text for values).

0.8 ± 0.04 mV; $n = 73$ spines for uncaging stimulation; Fig. 2*D*) to both uncaging and electrical stimuli. In fact, there was no statistical difference between the amplitude of uncaging potentials and physiological EPSPs in spines with neck lengths of less than 1.5 μm ($P = 0.31$) or larger than 1.5 μm ($P = 0.71$; Fig. 2*D*). Thus, our data indicated that, for activations of spines via either extracellular electrical stimulation or two-photon glutamate uncaging, the amplitude from the generated voltage response is inversely proportional to the spine neck length.

We further explored the database of 12 spines with minimal stimulation synaptic responses and found that the effect of the spine neck is independent of spine position, head dimensions, or Ca^{2+} accumulations in the spine head (Fig. S2; see *SI Text* for details).

Spine Neck Shortening Induced By Pairing Glutamate Uncaging and Action Potentials. Previous results have shown that the response amplitude of individual spines activated by two-photon glutamate uncaging—a technique that mimics transmitter release from a presynaptic neuron (Fig. S3) (31, 46)—is inversely proportional to the spine neck length, with long-necked spines having small or negligible somatic voltage contributions (31). By monitoring uncaging potentials at the soma, we sought to directly test whether the amplitude of individual spine synaptic potentials could be altered by inducing changes in spine neck length. To achieve this, we used a repetitive spike timing-dependent plasticity (STDP) protocol (47), in which two-photon uncaging of glutamate at a single spine (40×, every 2 s) was followed 15 ms later by back-propagating action potentials (bAPs; Fig. 3*A*). Using this protocol, we observed a significant shortening of the spine neck in both long- (Fig. 3*B*) and short-necked spines (Fig. 3*C*). This effect was observed in nine of 10 spines tested (30.48 ± 5.7% reduction from control, $n = 9$ spines; Fig. 4*A*). There was no correlation between spine neck length and percent reduction in neck length ($r = 0.046$, $P = 0.9$, $n = 9$ spines), indicating that spine neck plasticity occurs in short- and long-necked spines without any bias (range of spine neck lengths tested: 0.4–2 μm). Notably, one spine (of the 10 tested) experienced neck lengthening, rather than shortening, after the pairing protocol (43% change from control; Fig. 4*A*, single asterisk). The effect of the pairing protocol was specific to the spine being activated, because neighboring spines did not show any appreciable change in spine neck lengths (Fig. 3 *B3* and *C3*). Pairing uncaging with bAPs was necessary to generate morphological plasticity, because glutamate uncaging by itself did not result in any morphological changes (five of five spines, −1.29 ± 2.8% change from control; Fig. 4*C*, gray traces).

Increases in Uncaging Potential Amplitude After Spine Neck Shortening. To test if neck plasticity was accompanied by a change in the uncaging potentials generated at the spine, we analyzed the somatic voltage responses of these spines before and after the pairing protocol. In six of nine spines, shortening of the spine neck (30.91 ± 2.3% change, $n = 6$ spines) was accompanied by a significant enhancement in the amplitude of the uncaging potential (129.3 ± 68.04% increase from control, $P < 0.05$; Fig. 4 *A* and *B*; for individual examples; see Fig. 3 *B4* and *C4*). In two of the nine spines we detected smaller neck shortenings (11% change in both spines) with nonsignificant enhancements in the amplitude of uncaging potentials ($P = 0.73$ and $P = 0.6$; Fig. 4*A*). Finally, in the ninth spine, the one in which same pairing protocol induced a lengthening,

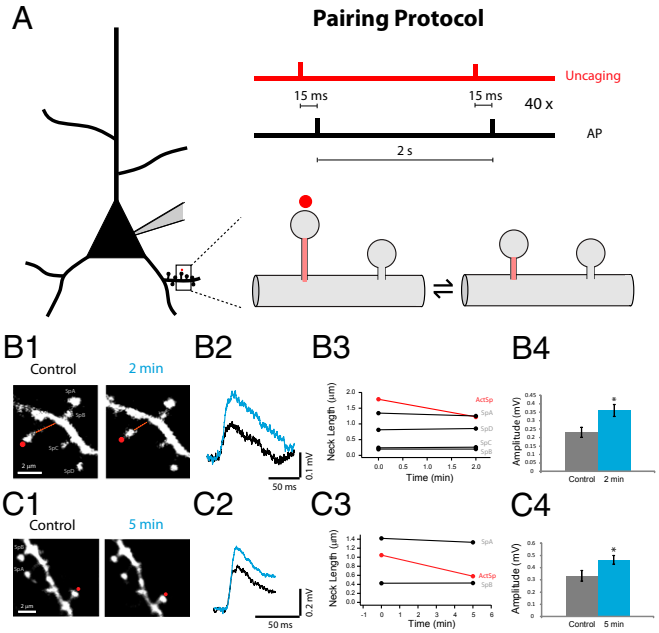

Fig. 3. Spine neck plasticity induced by pairing glutamate uncaging and bAPs. (*A*) Schematic of the experiment. (*B1*) Example of a long-necked spine before and after the pairing protocol. (*B2*) Average uncaging potentials from the spine in *B1* before (black) and after (blue) the pairing protocol. (*B3*) Neck-length changes in the stimulated spine (red) and in the four neighboring spines (black, SpA–D). (*B4*) Peak amplitude of the voltage responses before (black) and after (blue) the pairing protocol. $P < 0.05$ (*). (*C1*) Example of a spine with shorter neck than the one in *B*, before and after the pairing protocol. (*C2*) Average uncaging potentials from the spine in *C1* before (black) and after (blue) the pairing protocol. (*C3*). Neck-length changes in the stimulated spine (red) and in the two neighboring spines (black, SpA and B). (*C4*) Peak amplitude of the voltage responses before (black) and after (blue) the pairing protocol. *$P < 0.05$.

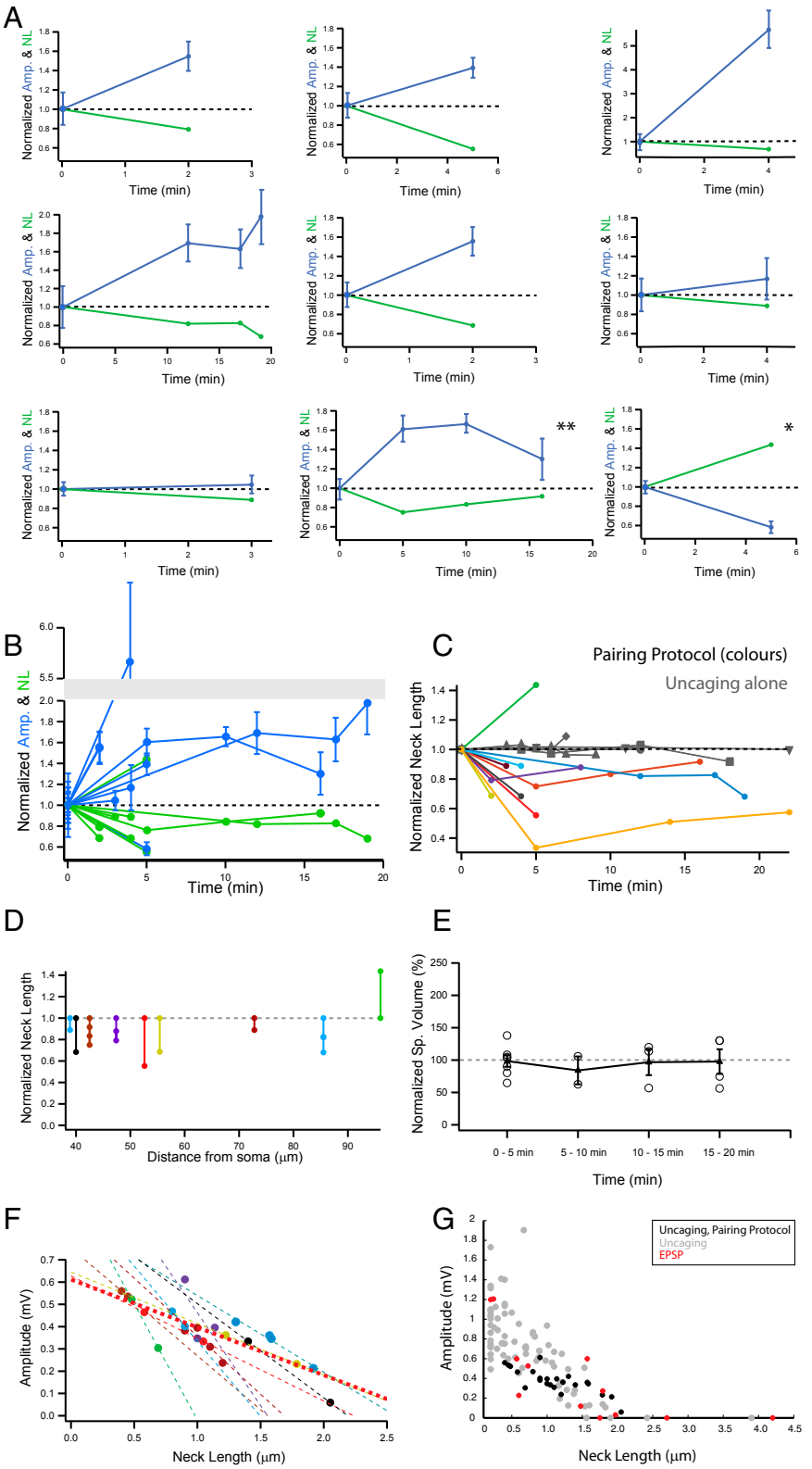

Fig. 4. Spine neck shortening after STDP is correlated with larger uncaging potentials. (*A*) Individual spine data: neck length and amplitude vs. time before (time 0) and after the pairing protocol. (*B*) Pooled data from *A*. (*C*) Time course of effect. Pooled data from spines that experienced both uncaging of MNI-glutamate and bAPs (colored markers), and those where only glutamate uncaging was triggered (gray markers). (*D*) Normalized neck length change in all spines vs. distance from soma. (*E*) Normalized spine volume change after pairing protocol. Data binned in different time points and average from each bin represented with a triangle ± SEM. (*F*) Amplitude of uncaging potential before and after pairing vs. the neck length. Each spine is represented with a different color. Lines represent linear fit to the data of individual experiments (dotted lines), and to pooled data (thicker dotted red line, see text for values). (*G*) Amplitude of the voltage response generated by glutamate uncaging (uncaging, gray circles), minimal stimulation voltage responses (EPSP, red circles), and uncaging responses from spines before and after the pairing protocol (uncaging, pairing protocol, black circles) vs. the neck length. Slopes of the three groups are not significantly different from each other ($P > 0.05$).

instead of a shortening, of the spine neck, the uncaging potential was smaller rather than larger in amplitude (Fig. 4*A*, asterisk; 43.75% neck length change from control and 41.77% reduction in the amplitude of the uncaging response: 0.52 ± 0.03 mV for control, $n = 30$ uncaging events and 0.3 ± 0.03 mV after 5 min of the paring protocol, $P < 0.001$). Overall, pooling the results from all spines, the pairing protocol generated a significant shortening of neck length (23.1 ± 9.03% reduction from control, $P < 0.001$, $n = 10$ spines) and a significant increase in the uncaging potential (123.5 ± 69.8% increase from control, $n = 9$ spines; $P < 0.05$). Moreover, for nine of nine spines, we observed an inverse correlation between changes in spine neck length and the amplitude of the uncaging potential. The morphological plasticity and concomitant changes in uncaging potentials lasted for as long as our measurements, with a temporal inverse correlation between changes in neck length and changes in uncaging responses (up to 20 min; $r = 0.79$, $P < 0.001$; Fig. 4 *B* and *F*). Finally, in one of the spines, the induced shortening of the spine neck partly reversed with time, and this reversal was accompanied by a similar increase and then subsequent decrease of the uncaging response (0.23 ± 0.02 mV under control conditions, $n = 29$ uncaging potentials; 0.38 ± 0.03 mV at 5 min, $n = 15$ events, $P < 0.001$ vs. control; 0.39 ± 0.02 mV at 10 min, $n = 30$ events, $P < 0.001$ vs. control; and 0.3 ± 0.04 mV at 16 min, $n = 15$ events, $P = 0.15$ vs. control; Fig. 4*A*, double asterisk).

Given that our paradigm involved bAPs generated at the soma and a tight temporal pairing protocol, we explored whether the distance of the activated spine to the soma affected those results. Interestingly, the spine whose stimulation led to lengthening of the neck and decrease in its uncaging potential was precisely the one located farthest away from the soma (Fig. 4*D*). Aside from that exception, there was no correlation between neck plasticity and distance from the soma in the other spines ($r = 0.22$, $P = 0.57$; Fig. 4*D*). We also explored whether this pairing protocol generated changes in spine head volume (47), but observed no significant change, as estimated from the FWHM of the fluorescence measured at the point where head diameter was largest (1.3 ± 8.4% change from control, $n = 10$; no statistical significance when compared against control conditions at different time bins: $P = 0.86$, 0.59, 0.88, and 0.91 for spines at 1–5, 5–10, 10–15, and 15–20 min after uncaging plus spikes; a linear regression of the spine volume vs. all times tested gave $r = 0.004$ and $P = 0.98$; Fig. 4*E*). Finally, we analyzed the relation between neck length and uncaging potential in individual synapses (Fig. 4*F*). Every spine displayed a negative correlation between neck length and uncaging potential amplitude, and the data from pooled spines displayed a significant negative correlation ($P < 0.001$; Fig. 4*F*, thick dotted red line). We compared these activity-dependent neck length changes and uncaging potential correlations with those observed following minimal stimulation of spines or with glutamate uncaging measurements in the absence of any pairing protocol. We found an excellent agreement between the three sets of data (Fig. 4*G*); all three datasets had negative correlations with slopes that were not significantly different from each other (all comparisons with $P > 0.05$, ANOVA).

Biophysical Simulations of the Effect of Spine Neck Plasticity. To understand the potential mechanisms responsible for the correlation between spine neck length and synaptic potentials, we turned to multicompartmental simulations. Using NEURON (48), we built a ball-and-stick model of a purely passive pyramidal neuron with one apical and two branching basal dendrites. On one of the basal dendrites we placed 200 stereotypical dendritic spines with morphologically realistic necks and heads (*Materials and Methods*). To simulate each experiment, we adjusted the membrane leak to produce experimentally observed input resistances and placed a single synaptic density in the spine head, located at the experimentally observed distance from the soma. Finally, we changed the dimensions of the spine head and neck to reflect its dimensions before and after the plasticity inducing protocol (STDP). We were thus able to constrain the parameters of our model sufficiently so that we could analyze the tradeoff between the two remaining variables that could affect the somatic EPSP—namely, the amplitude of the synaptic conductance g in the spine head and the resistivity of the spine neck ρ—and thus its resulting electrical resistance (Fig. 5*A*). In our simulations, we adjusted the resistivity of the spine neck ρ and used an automatic tuning protocol of the synaptic conductance g to reproduce the observed somatic EPSPs [Fig. 5 *B* and *C*; solid line in *C*: long-necked spine (pre-STDP), and dotted line in *C*: short-necked spine (post-STDP)]. We could then calculate the resistance value $R = \rho\, l/\mathrm{A}$, where l is the spine neck length and A is the electrically conducting cross-section of the spine neck (Fig. 5*D* and Fig. S4). It should be noted that the variable ρ may serve as a proxy variable for experimental details that were difficult to determine (e.g., the internal, electrically accessible cross-section of the spine neck). Similarly inspired modifications of spine neck diameter have been made in other models (32), and it is important to remember that the resulting resistance value (Fig. S5*A*) is the final goal of our considerations. Our numerical simulations revealed that it is possible to find solutions that can explain the observed correlation between the somatic EPSP amplitude and spine neck length (*i*) by varying synaptic conductance g and (*ii*) through purely electrotonic changes of the spine neck, i.e., a reduction of electrical resistance, that stem from its decreased neck length. A third possibility is combining an increase of synaptic conductance with additional neck passive voltage attenuation (Fig. 5 and Fig. S5*C*). For small neck resistivity values ρ [$<10^3$ Ωcm, and thus resistances of $R < 500$ MΩ for an average spine neck length (0.66 μm)] (5), there was virtually no electrotonic attenuation through the spine neck (Fig. 5*C*). Under these conditions, the synaptic event evoked only small voltage deflections at the spine head (<10 mV; Fig. 5*C*), and the voltage at the spine head and soma differed only by a factor equal to the dendritic attenuation. The experimentally observed transition from a long-necked spine with small somatic EPSP to a short-necked spine with larger somatic EPSP could only be explained by a substantial (50–450 nS) increase in synaptic conductance (Fig. 5 *E* and *F* and Fig. S5*C*). With increasing ρ ($>10^3$ Ωcm = $R > 500$ MΩ), the electrotonic passive attenuation properties of the spine neck were augmented. Larger synaptic conductances were necessary to produce the desired somatic EPSPs and hence also produced larger voltage deflections at the spine head (more pronounced at ρ values ~10^4 Ωcm, $R \sim 1$ GΩ; Fig. 5*C*). With increased neck resistivity values ρ, the electrotonic attenuation across the spine neck became more pronounced and accounted for a larger fraction of the somatic EPSP amplitude change observed after the transition from a long- to a short-necked spine (Fig. S5*C*). With increasing ρ values, the change in synaptic conductance g required to reproduce the experimental somatic EPSP observed after the STDP-dependent neck shrinkage (transition to a short-necked spine) decreased, until an identical pair of values for synaptic conductance g and neck ρ was reached that could explain both the pre-STDP (short-necked spine) and post-STDP (long-necked spine) somatic EPSPs simultaneously (Fig. 5 *C* and *D*; crossing point in *C*, numerical solution found in eight of nine spines). The crossing points at which the EPSP size transition observed experimentally between the long- and the short-necked spine (Fig. 5 and Fig. S4) can be attributed solely to the electrotonic or passive attenuation properties of the spine necks lie at relatively high spine neck resistance values, ranging between 1 and 12 GΩ, produced here by very high spine neck resistivity values because we assumed experimentally observed spine dimensions of length and (external) neck diameter (5) (see *Materials and Methods* and *Discussion*; Fig. 5*D* and Figs. S4 and S5). Though this might be the most parsimonious interpretation, it conflicts with evidence that

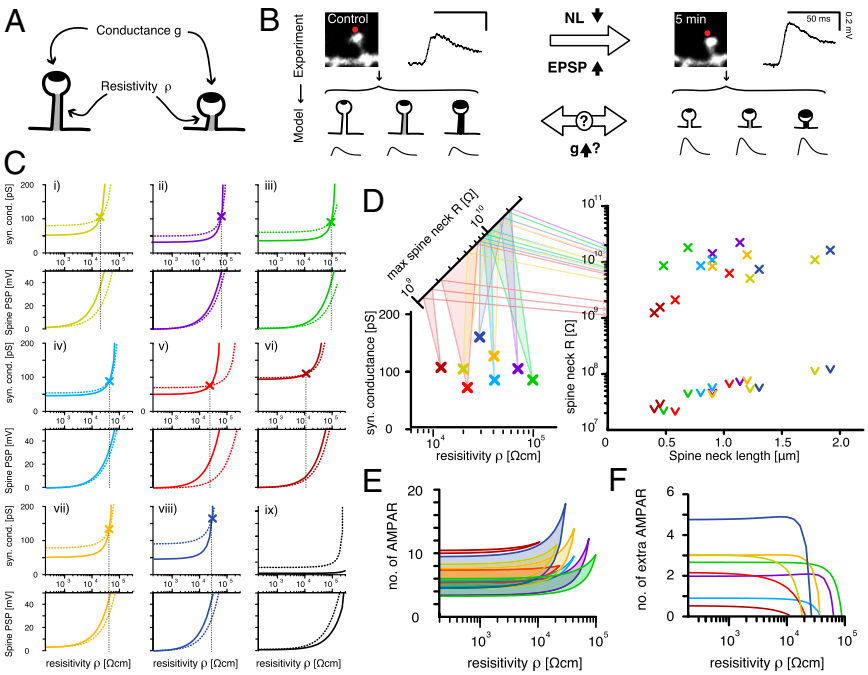

Fig. 5. Biophysical modeling of spine neck resistivity, resistance, and synapse conductance for spines before and after induction of STDP. (*A*) Starting from an experimentally constrained passive model of a cortical pyramidal cell, only two free parameters (neck resistivity ρ and synaptic conductance g) could affect the amplitude of the somatic EPSPs. (*B*) Schematic of the modeling approach. Several pairs of ρ/g values could be found to reproduce the experimentally observed EPSP amplitude values independently in long- and short-necked spines. (*C*) To investigate if a sole change in neck length was sufficient to produce the EPSP observed in each of the nine successful experiments (*i–ix*), we determined the correct synaptic conductance g in the short- and long-necked spine (dotted and solid lines, respectively, in *Upper* panels for each experiment) for a broad range of ρ values, and searched for a configuration in which both g and ρ were identical in both short- and long-necked spines (marked by an X and a dashed vertical line). (*C, i–ix, Lower*) Recorded evoked postsynaptic potential in the spine head (spine PSP) of both short- and long-necked spine (dotted and solid line, respectively). Notice that no single solution can be found for spine *ix*. (*D, Left*) Conductance (g) and resistivity (ρ) value pairs for experiments *i–viii* (color-coded to match crossing points from *C*) that explain the observed experimental phenomenon as a purely passive attenuation phenomenon. In addition, the calculated spine neck resistance for the pre-STDP long-necked spine and its post-STDP shortened neck form was calculated with each ρ value and reflected onto a second diagonal axis showing the actual spine neck resistance (R) of each individual spine, ranging from ~1 to 12 GΩ. (*Right*) Plot of the spine neck resistance (R) vs. spine neck length. Color-coded crosses mark the resistance values for short- and long-necked spine with the ρ value that allows for sole electrotonic attenuation in *C*. The arrowheads mark the R values for the lowest ρ values tested in *C*. (*E*) Estimated number of AMPA channels to produce the synaptic conductance of long- and short-necked spines for each resistivity value, based on an estimation of ~9-pS AMPA receptors. (*F*) The number of extra, new AMPA receptors required in the shortened spine to provide the additional synaptic conductance (after the induction of synaptic plasticity) that would also explain the result, but with lower resistivity values.

LTP involves changes in expression and activity of AMPA receptors (49). Notably, the membrane leak at the spine head (identical in value with the neuron-wide membrane leak) had only minimal effect, i.e., increasing or decreasing the leak conductance of the spine head did not shift the intersection point to qualitatively different results (Fig. S6).

We tested if we could rule out the high resistance solutions by performing simulations of bAPs and steady-state stimuli (SSS), but the voltage invasion of spine heads happened at low and high neck resistivity alike with little to no attenuation (Fig. S7 *A–C*). Even in long-necked spines with high resistivity values, only a small percentage drop (of up to 25% attenuation in bAP and 10% attenuation in SSS simulations, respectively) was observed.

These high resistivity values are higher than most recent estimates of spine neck resistance (~500 MΩ to 1 GΩ; Fig. S5 *A*, *B*, and *D*) (13, 32). If the neck resistance is indeed low, one could explain the observed spine neck plasticity and concomitant changes in EPSP size primarily through changes in synaptic conductance g, potentially mediated by an increase in the number of AMPA receptors. Indeed, the desired increase in peak conductance required only between four and 18 additional receptors for various neck resistivity ρ values, assuming a single-channel conductance of 9.25 pS (46) (Fig. 5*F*). Thus, even at low resistivity values, a small number of additional receptors could in many cases explain the observed ratio of EPSP amplitudes between long- and short- necked spines (Fig. 5*F*).

Discussion

In this study we first used a minimal stimulation protocol that did not trigger synaptic plasticity to address the question of whether the EPSPs generated by individual spines are correlated with their morphological features. Our results demonstrate that the activation of spines with longer necks produces EPSPs of smaller somatic amplitudes, in agreement with results obtained using glutamate uncaging (31). Intriguingly, long-necked spines do not appear to generate significant somatic depolarizations, even though they experience synaptic calcium accumulations. This inverse correlation between somatic voltage amplitude and spine neck length is present in the EPSP data and follows the same trend as the uncaging data (Fig. 2*C*) and the spine neck plasticity data (Fig. 4 *F* and *G*). Although many studies in the past have used similar minimal stimulation protocols in an effort to activate individual synaptic inputs (14, 18, 37–42), it is still possible that our extracellular minimal stimulation protocols activated more than one spine. Nevertheless, the fact that the minimal stimulation data, which was analyzed blind to the morphology of the spine, demonstrate a similar neck-length dependency as the uncaging data (where the presynaptic site is bypassed and a single spine is activated) suggests that the evoked voltage responses are likely

generated at the imaged spines. Moreover, the fact that long-necked spines generated synaptic calcium responses in their heads, even in the absence of somatic depolarizations, and that the amplitude range of these minimal responses was similar to measured single-input PSPs (14, 18, 31, 37, 43–46), likewise indicate that the imaged spines were the probable sites of the voltage responses.

In the second part of our study, we used a repetitive STDP protocol that triggers LTP (47), in which two-photon uncaging of glutamate at a single spine was closely followed by bAPs (Fig. 3*A*). Using this protocol, we induced significant changes in spine neck length while simultaneously monitoring the uncaging response of spines (Figs. 3 and 4). In a remarkable correlation without exception, every change in spine neck length is mirrored by an inverse change in spine uncaging potential, a correlation that is also temporally preserved (Fig. 4). This robust correlation could be a consequence of the effect of spine neck length on its resistance, or changes in synaptic conductance (Fig. 5; see below) or the recruitment of active conductances (36, 52–61). To explore these potential mechanisms we performed numerical simulations using data from spines obtained before and after the pairing protocol (Figs. 4 and 5 and Figs. S4 and S5). We tested whether the observed inverse correlation between EPSP amplitude and neck length can be accounted for by (*i*) variations of synaptic conductance *g*, (*ii*) electrotonic attenuation by high neck resistivity ρ, or (*iii*) a combination of the two. Our simulations demonstrate that it is possible to find solutions for all three scenarios, depending on the numerical values of the key variables (Fig. 5 and Figs. S4 and S5). Though a conductance change in a low spine-neck resistance scenario could explain this phenomenon, the voltages at the spine head, particularly those triggered during synaptic transmission (minimal synaptic stimulation or two-photon glutamate uncaging) in spines with short necks (Fig. 5*C*), may not be sufficient to significantly increase the probability of Mg^{2+} removal and unblocking of NMDA receptors, or to engage active conductances in the spine head, both of which have been shown to occur (13, 16–18, 32, 36). Solutions that rely exclusively on passive electrotonic attenuation (Fig. 5*C*, crossing point), however, do not require additional synaptic conductance *g* but assume high axial neck resistivity ρ values (between 10^4 and 10^5 Ωcm) or, alternatively, that a majority of the spine neck's cross-section is not electrically conducting (*Materials and Methods*). The resulting high neck resistance values (between 1 and 12 GΩ; Fig. 5*D* and Fig. S4) differ from recent estimates of spine neck resistance [~0.5 MΩ (32) up to 1GΩ (13)] (Fig. S5*B*). One possible scenario is that in spines with a neck resistance high enough to produce voltage deflections at the spine head that can remove Mg^{2+} block from NMDA receptors and activate voltage-gated channels, quick changes in synaptic conductance (on the order of a few additional channels; Fig. 5 *E* and *F*) are a major contributor to the changes in synaptic strength in response to our pairing plasticity protocol. Such a mixed scenario—with a large voltage drop along the neck, amplification of spine head EPSPs, and activation of voltage-dependent conductances—could potentially interfere with a Hebbian mechanism. However, the lack of direct techniques to accurately measure absolute spine potentials and neck resistivity prevent us at this point from completely ruling out pure changes in synaptic conductance or neck resistance. Furthermore, simple voltage-divider principles can also capture the essence of the inverse correlation between somatic EPSPs and neck length, and assume that the relative effectiveness of a synapse on a spine compared with one directly on the shaft is giving by $1/(1 + P)$ (*Materials and Methods*), where *p* is the product of spine neck resistance and the synaptic conductance. This calculation reveals (as confirmed by our detailed simulations) that provided $P < 1$, there should be no effect of neck resistance on somatic EPSP (for a fixed soma–spine distance), and that for $P > 1$, the somatic EPSP and the neck length should be reciprocally related. Our data imply that $P \sim 1$, and therefore confirm other recent data suggesting that neck resistance is appreciable. However, it is not possible to be more precise given current ignorance about the (presumably variable) values for synaptic conductance and neck resistance. For all these reasons, we are agnostic at this point as to the exact biophysical mechanisms that underlie the phenomenology we present.

The regulation of synaptic strength by rapid changes in spine neck length was first proposed by Rall (53) as a potential mechanism for rapid synaptic plasticity. Our results are consistent with this early proposal because they demonstrate an inverse correlation between spine neck length and synaptic strength, but appear at odds with recent results, in which repetitive stimulation of spines with similar pairing protocols lead to increases in spine head volume (47). We did not observe increases in head volume after the pairing protocol (Fig. 4*E*), perhaps due to methodological differences, because our data were taken from mouse neocortical neurons, using ACSF with physiological concentrations of Mg^{2+} and intracellular solutions without actin. In fact, the addition of actin as used by Tanaka et al. (47) (5-μM actin in the intracellular solution) was reported crucial for the spine head enlargement to occur, and may be the critical difference to our protocol; this is particularly relevant because it may have allowed us to specifically dissect the spine neck plasticity effect observed after STDP and its effect on synaptic strength. We also only monitored the morphology of spines for up to 20 min after the pairing protocol, and it is possible that increases in head diameter occur later and that both changes in neck length and head size are at works. Indeed, in the analysis of data from spines of similar neck lengths, we observe a statistical correlation between spine head diameter and uncaging potentials ($r = 0.87$, $P < 0.001$, $n = 11$ spines with 0.2-μm neck length), consistent with previous reports (21, 47, 54, 55). Thus, we think that it is likely that the spine neck length and its diameter, together with the spine head size, are morphological correlates of synaptic strength, highlighting the close relation between spine structure and function in the CNS. Indeed, a recent study using superresolution-stimulated emission depletion and an uncaging LTP protocol has shown that activated spines undergo changes in spine head, neck length, and neck diameter (56). In addition, further research aimed at the molecular spine machinery (57, 58) behind the STDP-dependent spine neck dynamics will need to be conducted.

In summary, our results demonstrate that spike-timing stimulation paradigms can induce synaptic potentiation and selectively shorten the length of the spine neck (Figs. 3 and 4), thus providing, to our knowledge, the first functional correlation between activity-dependent spine neck changes and the regulation of synaptic strength. We also describe how spines with long necks apparently have little functional effect on the soma of a neuron, raising the issue of what their function may be. The solution may lie precisely in their behavior that we observe after STDP, where they become shorter and functionally connected to the soma of the neuron. Long-necked spines, like short-necked spines, are invaded by bAPs (31, 36, 59, 60). Indeed, our simulations showed that bAPs and steady-state stimuli (Fig. S7) invade spine heads at all tested neck lengths and values of ρ and *R*, with no attenuation in most of the conditions tested and only a small percentage reduction of the voltage signal (up to ~25% and 10% attenuation of the bAP and SSS, respectively), even in long-necked spines with values of neck resistivity ρ (at odds with estimates) that can contribute significantly to EPSP size control (Fig. S7). The observed neck shortening may allow changes in functional connectivity onto a postsynaptic cell without the need to physically rewire the network. Interestingly, these long-necked spines are particularly prominent in human cortical circuits (61) and could represent an important connectivity reservoir for the rapid and activity-dependent control of synaptic strength.

Materials and Methods

Brain Slice Preparation and Electrophysiology. Brains from postnatal day 13–16 C57BL/6 mice of either sex were removed and immersed in cold cutting solution containing (in mM): 27 $NaHCO_3$, 1.5 NaH_2PO_4, 222 sucrose, 2.6 KCl, 1 $CaCl_2$, 3 $MgSO_4$, and equilibrated with 95% O_2/5% CO_2. Coronal brain slices (300 μm thick) of visual cortex were prepared using a Leica VT1200S Vibratome and transferred to a chamber with ACSF containing (in mM): 126 NaCl, 26 $NaHCO_3$, 10 dextrose, 1.15 NaH_2PO_4, 3 KCL, 2 $CaCl_2$, 2 $MgSO_4$, and oxygenated with 95%O_2/5% CO_2 at 37 °C for 30 min, and then incubated at room temperature for at least 40 min before recording. Electrophysiological recordings were performed in whole-cell current–clamp configuration with MultiClamp 700B amplifiers (Axon) with patch electrodes (4–7 MΩ) filled with internal solution containing (in mM): 135 $KMeSO_4$, 10 KCl, 10 Hepes, 5 NaCl, 2.5 Mg-ATP, 0.3 Na-GTP, and 0.2 Alexa Fluor 488. Resting membrane potential was held at −65 mV. All experiments were conducted at 37 °C.

Two-Photon Fluorescence Imaging and Uncaging of Glutamate. Imaging was done with a custom-made two-photon laser-scanning microscope, consisting of a modified Olympus FluoView FV-200 system (side-mounted to a BX50WI microscope with a 60×, 0.9 N.A., water-immersion objective) and a tunable Ti:Sapphire laser (Chameleon Ultra II, Coherent, >3 W, 140-fs pulses, 80 MHz repetition rate). Fluorescence was detected with a photomultiplier tube (PMT) (H7422-P40; Hamamatsu) connected to a signal amplifier (Signal Recovery AMETEK Advanced Measurement Technology) whose output was connected to the FluoView system. Fluorescence images of the soma, dendrites, and dendritic spines were acquired with FluoView software (XY scan mode with 1× to 10× digital zoom) at 725 nm, and calcium fluorescence was acquired at 820 nm. Axial stacks were taken every 0.4 μm. Distances of the spines to the soma, spine head diameters (longest possible axis in any frame in the z-stack of images), and neck lengths, measured from the proximal edge of the spine head to the edge of the dendrite, were measured using ImageJ (National Institutes of Health). The segmented line selection tool in ImageJ was used to measure the neck length, including any resolved curvature. With the use of fluorescence microspheres (0.1 μm diameter), we calculated the diffraction-limited resolution of our two-photon microscope. The FWHM in *x*, *y*, and *z* axis is 0.393, 0.378, and 1.714 μm, respectively—similar to the theoretical resolution of 0.328 μm for *x* and *y*, and 1.148 μm for *z* at 820-nm excitation and objective N.A. of 1.0. Due to this limitation in those spines with no discernible necks, we chose a minimum neck length value of 0.2 μm. In addition, if a small neck curvature or angle of departure of the neck from the parent dendrite is present and below the diffraction limited resolution of our microscope, then in those spines we will have an underrepresentation of the actual spine neck length. Spine head volume was measured using the FWHM to calculate the diameter of the spine head. The spine head volume was then estimated as $4/3\pi r^3$, as previously reported (21). An estimated value for the radius of the spine head, *r*, was obtained based on the measured FWHM diameter of the spine.

Two-photon uncaging of 4-methoxy-7-nitroindolinyl (MNI)-caged L-glutamate (2.5 mM; Tocris Cookson) was performed as described (31). Uncaging was performed at 725 nm. Here we reported 24 new spine uncaging potentials that were added to the previously reported uncaging data set ($n = 58$; total = 82 spine uncaging potentials; gray dots in Figs. 2*C* and 4*G*) (31). All recordings were performed in the most superficial portions of the brain slices (<100 μm deep).

The location of the uncaging spot was positioned in approximately the same location along the edge of the spine head before and after the paring protocol (Fig. 3) and at a location where no glutamate spillover to the shaft affected our observations (Fig. S3*B*). Moreover, slight movements of the uncaging spot along the edge of the spine head do not cause any significant changes in the evoked voltage responses that we recorded at the soma (Fig. S3*A*).

Electrical Stimulation of Spines. Neurons were filled with Alexa 488 (200 μM) and fluo-4 (200 μM). A stimulating electrode, filled with Alexa 594 dextran dye (10,000 MW, 50 μM), was located close (~4–20 μm) to the spine head. Short stimulating pulses (20 μs duration and 10–15 pulses per spine at 0.5 Hz) were delivered to the stimulating electrode via an Iso-flex stimulator (AMPI) while the calcium signals were recorded using a PMT to collect the fluorescence signal arising from line scans intersecting the spine head. We recorded activity from spines located between 11 and 100 μm from the soma.

Analysis of Minimal Stimulation Responses. To guarantee an unbiased analysis of the minimal stimulation responses from individual spines, we devised a method that used a custom-made MATLAB script to identify calcium responses and to measure the amplitude of their concurrent EPSPs. This method automatically scored the successes and failures of the voltage responses and their corresponding spine calcium accumulations (Fig. S1). For this purpose, the peak of the calcium response at the spine head (measured as %ΔF/F) and the peak amplitude and 10–90% rate of rise of the concomitant somatic voltage responses were automatically measured, and a database of all positive and negative calcium responses with their corresponding voltage traces was assembled (22 different spines, 16 neurons). First, raw calcium imaging sweeps were cropped around the investigated spine and filtered with a standard Gaussian low-pass filter with a 1.5-μm radius (Fig. S1 *A* and *B*). For the automatic analysis program to detect a positive spine calcium signal, three statistical criteria had to be independently met (Fig. S1): (*i*) The peak amplitude of the calcium responses (the average signal amplitude of a 5-ms window centered on the maximum of the signal within the first 50 ms after the stimulus) had to be at least 2.5× greater than the SD of the baseline signal before the stimulus (Fig. S1*D*); (*ii*) A significant statistical difference (determined by a Student's *t* test at 99% level of confidence) had to be found between the baseline (data points from −50 to 0 ms, where 0 ms marks the occurrence of the stimulus) and the afterstimulus (from +10 to +60 ms) of the calcium signal (Fig. S1*D*, shaded green); and (*iii*) The shape of the first 100 ms of the signal after the stimulus could be fit agreeably to a double exponential with previously determined time constants tau1 (t1) = 60 ms and tau2 (t2) = 100 ms (Fig. S1 *A*–*C*). The concurrent voltage traces were analyzed independently. The amplitude of each EPSP was determined as the difference of the averages of two 5-ms time windows, one centered on −3 ms before the stimulus and the other on the maximum voltage deflection within 50 ms after the stimulus occurred (Fig. S1*E*). To measure the rate of rise of nonzero EPSPs, the difference between the times and the voltage, when the membrane potential reached 10% and 90% of the maximum voltage deflection, was measured, and the rate of rise (in mV/ms) calculated (Fig. S1*E*). Afterward, the positive calcium responses that met these three criteria were measured and their corresponding EPSPs measured. Then, from those positive calcium trials, only the trial with the minimum of all EPSPs, or the zero-voltage response associated with it were determined and further analyzed. Thus, we had positive calcium signals that were associated with a zero-voltage response and calcium signals associated with voltage responses. In the latter, only if this candidate EPSP was the minimal nonzero EPSP associated with a positive calcium signal at the spine head, was the event recorded as the minimal elicited response; this was done to exclude the possibility of recording erroneous multispine events as single synaptic events.

The time constants of the double-exponential kernel function used to test single-trial calcium responses as described above were derived from the average response of five single-trial spine stimulations with high signal-to-noise ratios of the recorded calcium response (Fig. S1*A*). We filtered the resulting average response with a standard Gaussian low-pass filter (Fig. S1*B*) with a 1.5-μm radius and fitted the mean response of the spine head to a double-exponential function of the form

$$y(t) = c \times (\exp(-t/\text{tau1}) - \exp(-\text{dt}/\text{tau2}))/(\text{tau } 1 - \text{tau } 2),$$

in which tau1 = 60 ms and tau2 = 100 ms produced the best fit.

We then adjusted *c* to optimally fit the original five traces with identical tau1 and tau 2 and used the resulting rmse values between the fit and the data as a measure for thresholding what was an "agreeable fit," as discussed above. Consequently, any fit that produced an rmse less than or equal to 1.5× the maximum rmse of the calibration traces was accepted as a good fit.

Pairing Protocol. To induce spine neck plasticity, we used repetitive two-photon uncaging of MNI-glutamate—40 times every 2 s—with each uncaging pulse (2-ms duration) followed after 15 ms by a postsynaptic spike (Fig. 3*A*). The two-photon uncaging response of the spines, tested before and after the pairing protocol, was assessed as previously described (31). When more than one time point after the pairing protocol was imaged from the tested spine, the maximal change in neck length from the time points recorded was used to calculate the percentage change value for further comparisons with the other experiments.

Analysis was conducted using MatLab or IGOR Pro with Neuromatic v2.0 package. All measurements are expressed as ± SEM. Statistical significance was assessed using Student *t* test and Kolmogorov–Smirnov test when appropriated at the significance level (*P*) indicated. Correlations between morphological and physiological parameters were fitted with a linear regression. In addition, to capture the essence of the relation between the somatic EPSP and neck resistance (R_{neck}), we used the voltage divider equation (62) to arrive at a simplified formula that represents the relative

effectiveness of a synapse on a spine compared with one directly on the parent dendritic shaft, and with which we fit the experimental data on the correlation between EPSP and neck length presented in Fig. 2*C*:

$$\frac{EPSPdend(sp)}{EPSPdend(dend)} = \frac{1}{1+P}, \quad [1]$$

where P is the product of the synaptic conductance (G_{syn}) and R_{neck}, $EPSP_{dend(sp)}$ is the amplitude of the voltage generated in the dendrite at the place where the spine is attached after a synapse is impinged onto a spine, and $EPSP_{dend(dend)}$ is the amplitude of the voltage in the dendrite when the synapse is located in the dendrite. These formulas are

$$EPSP_{dend(sp)} = E_{syn} \times \frac{Rdend}{\frac{1}{Gsyn} + Rneck + Rdend} \quad [2]$$

$$EPSP_{dend(dend)} = E_{syn} \times \frac{Rdend}{\frac{1}{Gsyn} + Rdend} \quad [3]$$

With R_{dend} representing the input resistance of the dendrite at the place where the spine is attached to the dendrite; *Gsyn*, the synaptic conductance; *Rneck*, the spine neck resistance; and *Esyn*, the resting membrane potential. For simplicity, in Eq. **1** we assumed a negligible value of R_{dend}. This fit reveals that provided $P < 1$ there should be no effect of R_{neck} on somatic EPSPs (for a fixed soma–spine distance), and that for $P > 1$, the somatic EPSP and the neck length should be reciprocally related. This fit assumes a purely passive attenuation of spine potentials.

Methods for the Numerical Simulations. To investigate the potential mechanisms behind the correlation between spine neck length and synaptic potentials obtained before and after the induction of synaptic plasticity, we built a NEURON model with the simplified morphology of a layer-5 pyramidal cell. The model consisted of a 20-μm–diameter soma with one apical and two basal dendrites. The apical dendrite was a simple cable measuring 3 μm in diameter and 300 μm in length with no daughter branches. The basal dendrites consisted of 1-μm–wide, 200-μm–long cables with two daughter branches, 170 μm and 80 μm long, branching out at 30 μm and 120 μm, respectively. We constructed 190 spines and placed them equidistant from each other on the main branch of one basal dendrite. Each spine consisted of a spine neck and a spine head. Initially, the dimensions of these compartments were set to the reported average values (4): 0.66-μm spine neck length, 0.2-μm spine neck diameter, and 1-μm spine head diameter. The membrane capacity of the whole neuron was uniformly set to 1 μF/cm^2. To investigate the possible combinations of synaptic conductance and spine neck resistivity that could have led to the results reported in Figs. 3 and 4, we reproduced the conditions of each recorded spine in the model. The resting membrane potential was set to −65 mV and the membrane resistance was initially adjusted to R_M = 4,700 Ωcm^2, which sets the input resistance, measured by a −10 pA, 100-ms input current delivered to the soma, to 150 MΩ. We then adjusted R_M in each model cell to reproduce the input resistance recorded at the soma of each of the nine recorded experiments, ranging from 82 to 221 MΩ. The neck length of a single spine at the correct distance from the soma (as recorded in each experiment) was adjusted to fit with the initially recorded neck length. A single conductance based synapse in the form of an α function (with tau g = 10 ms, resulting in 80- to 100-ms-long EPSPs) was introduced to the spine. To change the resistance of the neck (and, notably, not any other parts of the neuron), its resistivity was varied between 2×10^2 and 10^6 Ωcm, and for each resistivity value, simulations were run in which the amplitude of the synaptic conductance was tuned to achieve a somatic voltage deflection equal to the experimentally recorded somatic EPSP. In a second step, the spine neck was shortened and its diameter was widened (26, 56) to keep the membrane area of the neck constant. The tuning protocol was repeated and the conductance values were recorded. To estimate the number of AMPA receptors required to create the peak voltage deflection recorded at the soma, we estimated the AMPA receptor unitary conductance (γ) to be 9.25 pS per AMPA receptor—based on the mean AMPA receptor unitary current obtained from nonstationary fluctuation analyses from EPSCs triggered by two-photon uncaging of glutamate over single spines from CA1 pyramidal neurons (46)—and divided the observed necessary synaptic conductance by γ. The AMPA receptor unitary conductance calculated from Matsuzaki et al. (46) is very similar to the values reported after synaptic activation in CA1 pyramidal neurons (63).

To assess voltage invasion for a steady-state stimulus, we injected a 40-ms current pulse of 0.3 nA into the soma of the neuron and recorded the maximum voltage deflection at the spine head as well as at the dendrite adjacent to the spine of interest. Similarly, to assess bAP voltage invasion of the spine, we added a set of Hodgkin–Huxley-type ion channels to the soma and evoked action potentials with a short current pulse.

We calculated the contribution of the voltage attenuation based on the Δ EPSP between long- and short-necked spines in the absence of changes in conductance g, normalized by the experimentally observed Δ EPSP.

ACKNOWLEDGMENTS. We thank members of R.Y.'s laboratory, and in particular Dr. Alan Woodruff, for help and comments, and Dr. Darcy Peterka for optical and technical advice. Financial support was provided by the Pew Charitable Trust, a Pew Latin American Fellowship (to R.A.), National Institute of Neurological Disorders and Stroke Grant R21NS081393, National Institute on Drug Abuse Grant R21DA034195, a Patterson Trust Fellowship (to T.P.V.), and European Community's Seventh Framework Marie Curie International Reintegration Grant 268436 (T.P.V.). This material is based upon work supported by, or in part by, the US Army Research Laboratory and the US Army Research Office Contract W911NF-12-1-0594 (Multidisciplinary University Research Initiative).

1. Ramón y Cajal S (1899) *La Textura del Sistema Nerviosa del Hombre y los Vertebrados* (Moya, Madrid).
2. Gray EG (1959) Electron microscopy of synaptic contacts on dendrite spines of the cerebral cortex. *Nature* 183(4675):1592–1593.
3. Colonnier M (1968) Synaptic patterns on different cell types in the different laminae of the cat visual cortex. An electron microscope study. *Brain Res* 9(2):268–287.
4. Arellano JI, Benavides-Piccione R, DeFelipe J, Yuste R (2007) Ultrastructure of dendritic spines: Correlation between synaptic and spine morphologies. *Front Neurosci* 1(1): 131–143.
5. Arellano JI, Espinosa A, Fairén A, Yuste R, DeFelipe J (2007) Non-synaptic dendritic spines in neocortex. *Neuroscience* 145(2):464–469.
6. Harris KM (1999) Structure, development, and plasticity of dendritic spines. *Curr Opin Neurobiol* 9(3):343–348.
7. Chen JL, et al. (2012) Clustered dynamics of inhibitory synapses and dendritic spines in the adult neocortex. *Neuron* 74(2):361–373.
8. Shepherd GM (1996) The dendritic spine: A multifunctional integrative unit. *J Neurophysiol* 75(6):2197–2210.
9. Yuste R (2010) *Dendritic Spines* (MIT Press, Cambridge, MA).
10. Harris KM, Kater SB (1994) Dendritic spines: Cellular specializations imparting both stability and flexibility to synaptic function. *Annu Rev Neurosci* 17:341–371.
11. Svoboda K, Tank DW, Denk W (1996) Direct measurement of coupling between dendritic spines and shafts. *Science* 272(5262):716–719.
12. Majewska A, Tashiro A, Yuste R (2000) Regulation of spine calcium dynamics by rapid spine motility. *J Neurosci* 20(22):8262–8268.
13. Bloodgood BL, Sabatini BL (2005) Neuronal activity regulates diffusion across the neck of dendritic spines. *Science* 310(5749):866–869.
14. Yuste R, Denk W (1995) Dendritic spines as basic functional units of neuronal integration. *Nature* 375(6533):682–684.
15. Denk W, Sugimori M, Llinás R (1995) Two types of calcium response limited to single spines in cerebellar Purkinje cells. *Proc Natl Acad Sci USA* 92(18):8279–8282.
16. Kovalchuk Y, Eilers J, Lisman J, Konnerth A (2000) NMDA receptor-mediated subthreshold Ca(2+) signals in spines of hippocampal neurons. *J Neurosci* 20(5):1791–1799.
17. Koester HJ, Sakmann B (1998) Calcium dynamics in single spines during coincident pre- and postsynaptic activity depend on relative timing of back-propagating action potentials and subthreshold excitatory postsynaptic potentials. *Proc Natl Acad Sci USA* 95(16):9596–9601.
18. Yuste R, Majewska A, Cash SS, Denk W (1999) Mechanisms of calcium influx into hippocampal spines: Heterogeneity among spines, coincidence detection by NMDA receptors, and optical quantal analysis. *J Neurosci* 19(6):1976–1987.
19. Holmes WR (1990) Is the function of dendritic spines to concentrate calcium? *Brain Res* 519(1-2):338–342.
20. Koch C, Zador A (1993) The function of dendritic spines: Devices subserving biochemical rather than electrical compartmentalization. *J Neurosci* 13(2):413–422.
21. Matsuzaki M, Honkura N, Ellis-Davies GC, Kasai H (2004) Structural basis of long-term potentiation in single dendritic spines. *Nature* 429(6993):761–766.
22. Chang HT (1952) Cortical neurons with particular reference to the apical dendrites. *Cold Spring Harb Symp Quant Biol* 17:189–202.
23. Rall W (1974) Dendritic spines, synaptic potency and neuronal plasticity. *Cellular Mechanisms Subserving Changes in Neuronal Activity*, eds Woody CD, et al. (Brain Information Services, Los Angeles), pp 13–21.
24. Jack JJB, Noble D, Tsien RW (1975) *Electric Current Flow in Excitable Cells* (Oxford Univ Press, London).
25. Llinás R, Hillman DE (1969) Physiological and morphological organization of the cerebellar circuits in various vertebrates. *Neurobiology of Cerebellar Evolution and Development*, ed Llinas R (American Medical Assoc Education and Research Foundation, Chicago), pp 43–73.
26. Koch C, Poggio T (1983) Electrical properties of dendritic spines. *Trends Neurosci* 6:80–83.
27. Miller JP, Rall W, Rinzel J (1985) Synaptic amplification by active membrane in dendritic spines. *Brain Res* 325(1-2):325–330.

28. Segev I, Rall W (1988) Computational study of an excitable dendritic spine. *J Neurophysiol* 60(2):499–523.
29. Tsay D, Yuste R (2004) On the electrical function of dendritic spines. *Trends Neurosci* 27(2):77–83.
30. Yuste R (2011) Dendritic spines and distributed circuits. *Neuron* 71(5):772–781.
31. Araya R, Jiang J, Eisenthal KB, Yuste R (2006) The spine neck filters membrane potentials. *Proc Natl Acad Sci USA* 103(47):17961–17966.
32. Harnett MT, Makara JK, Spruston N, Kath WL, Magee JC (2012) Synaptic amplification by dendritic spines enhances input cooperativity. *Nature* 491(7425):599–602.
33. Bloodgood BL, Giessel AJ, Sabatini BL (2009) Biphasic synaptic Ca influx arising from compartmentalized electrical signals in dendritic spines. *PLoS Biol* 7(9):e1000190.
34. Rose CR, Kovalchuk Y, Eilers J, Konnerth A (1999) Two-photon Na+ imaging in spines and fine dendrites of central neurons. *Pflugers Arch* 439(1-2):201–207.
35. Grunditz A, Holbro N, Tian L, Zuo Y, Oertner TG (2008) Spine neck plasticity controls postsynaptic calcium signals through electrical compartmentalization. *J Neurosci* 28(50):13457–13466.
36. Araya R, Nikolenko V, Eisenthal KB, Yuste R (2007) Sodium channels amplify spine potentials. *Proc Natl Acad Sci USA* 104(30):12347–12352.
37. Conti R, Lisman J (2003) The high variance of AMPA receptor- and NMDA receptor-mediated responses at single hippocampal synapses: Evidence for multiquantal release. *Proc Natl Acad Sci USA* 100(8):4885–4890.
38. Emptage N, Bliss TV, Fine A (1999) Single synaptic events evoke NMDA receptor-mediated release of calcium from internal stores in hippocampal dendritic spines. *Neuron* 22(1):115–124.
39. Enoki R, Hu YL, Hamilton D, Fine A (2009) Expression of long-term plasticity at individual synapses in hippocampus is graded, bidirectional, and mainly presynaptic: optical quantal analysis. *Neuron* 62(2):242–253.
40. Malinow R, Otmakhov N, Blum KI, Lisman J (1994) Visualizing hippocampal synaptic function by optical detection of Ca2+ entry through the N-methyl-D-aspartate channel. *Proc Natl Acad Sci USA* 91(17):8170–8174.
41. Oertner TG, Sabatini BL, Nimchinsky EA, Svoboda K (2002) Facilitation at single synapses probed with optical quantal analysis. *Nat Neurosci* 5(7):657–664.
42. Toni N, et al. (2007) Synapse formation on neurons born in the adult hippocampus. *Nat Neurosci* 10(6):727–734.
43. Kalisman N, Silberberg G, Markram H (2005) The neocortical microcircuit as a tabula rasa. *Proc Natl Acad Sci USA* 102(3):880–885.
44. Bolshakov VY, Siegelbaum SA (1995) Regulation of hippocampal transmitter release during development and long-term potentiation. *Science* 269(5231):1730–1734.
45. Losonczy A, Magee JC (2006) Integrative properties of radial oblique dendrites in hippocampal CA1 pyramidal neurons. *Neuron* 50(2):291–307.
46. Matsuzaki M, et al. (2001) Dendritic spine geometry is critical for AMPA receptor expression in hippocampal CA1 pyramidal neurons. *Nat Neurosci* 4(11):1086–1092.
47. Tanaka J, et al. (2008) Protein synthesis and neurotrophin-dependent structural plasticity of single dendritic spines. *Science* 319(5870):1683–1687.
48. Hines ML, Carnevale NT (1997) The NEURON simulation environment. *Neural Comput* 9(6):1179–1209.
49. Malenka RC, Bear MF (2004) LTP and LTD: An embarrassment of riches. *Neuron* 44(1): 5–21.
50. Burkhalter A, Gonchar Y, Mellor RL, Nerbonne JM (2006) Differential expression of I(A) channel subunits Kv4.2 and Kv4.3 in mouse visual cortical neurons and synapses. *J Neurosci* 26(47):12274–12282.
51. Lai HC, Jan LY (2006) The distribution and targeting of neuronal voltage-gated ion channels. *Nat Rev Neurosci* 7(7):548–562.
52. Paspalas CD, Wang M, Arnsten AF (2013) Constellation of HCN channels and cAMP regulating proteins in dendritic spines of the primate prefrontal cortex: Potential substrate for working memory deficits in schizophrenia. *Cereb Cortex* 23(7):1643–1654.
53. Rall W (1974) Dendritic spines and synaptic potency. *Studies in Neurophysiology*, ed Porter R (Cambridge Univ Press, Cambridge, UK), pp 203–209.
54. Harvey CD, Svoboda K (2007) Locally dynamic synaptic learning rules in pyramidal neuron dendrites. *Nature* 450(7173):1195–1200.
55. Lee SJ, Escobedo-Lozoya Y, Szatmari EM, Yasuda R (2009) Activation of CaMKII in single dendritic spines during long-term potentiation. *Nature* 458(7236):299–304.
56. Tønnesen J, Katona G, Rózsa B, Nägerl UV (2014) Spine neck plasticity regulates compartmentalization of synapses. *Nat Neurosci* 17(5):678–685.
57. Charrier C, et al. (2012) Inhibition of SRGAP2 function by its human-specific paralogs induces neoteny during spine maturation. *Cell* 149(4):923–935.
58. Ryu J, et al. (2006) A critical role for myosin IIb in dendritic spine morphology and synaptic function. *Neuron* 49(2):175–182.
59. Holthoff K, Zecevic D, Konnerth A (2010) Rapid time course of action potentials in spines and remote dendrites of mouse visual cortex neurons. *J Physiol* 588(Pt): 1085–1096.
60. Palmer LM, Stuart GJ (2009) Membrane potential changes in dendritic spines during action potentials and synaptic input. *J Neurosci* 29(21):6897–6903.
61. Benavides-Piccione R, Ballesteros-Yáñez I, DeFelipe J, Yuste R (2002) Cortical area and species differences in dendritic spine morphology. *J Neurocytol* 31(3-5):337–346.
62. Johnston D, Wu S (1995) *Foundations of Cellular Neurophysiology* (MIT Press, Cambridge, MA).
63. Benke TA, Lüthi A, Isaac JT, Collingridge GL (1998) Modulation of AMPA receptor unitary conductance by synaptic activity. *Nature* 393(6687):793–797.